




Superior ultra-thin nanoporous g-C₃N₄ photocatalyst embedded with S quantum dots: a non-metal Z-scheme visible-light composite

Yimeng Wang¹, Hecheng Ma¹, Jianjun Liu^{1,*} , Yingchun Yu¹, Shengli Zuo¹, Xiangdong Zhang¹, and Shuxiang Zheng¹

¹ State Key Laboratory of Chemical Resource Engineering, Beijing University of Chemical Technology, Beijing 100029, People's Republic of China

Received: 19 August 2021

Accepted: 11 October 2021

Published online:
3 January 2022

© The Author(s), under exclusive licence to Springer Science+Business Media, LLC, part of Springer Nature 2021

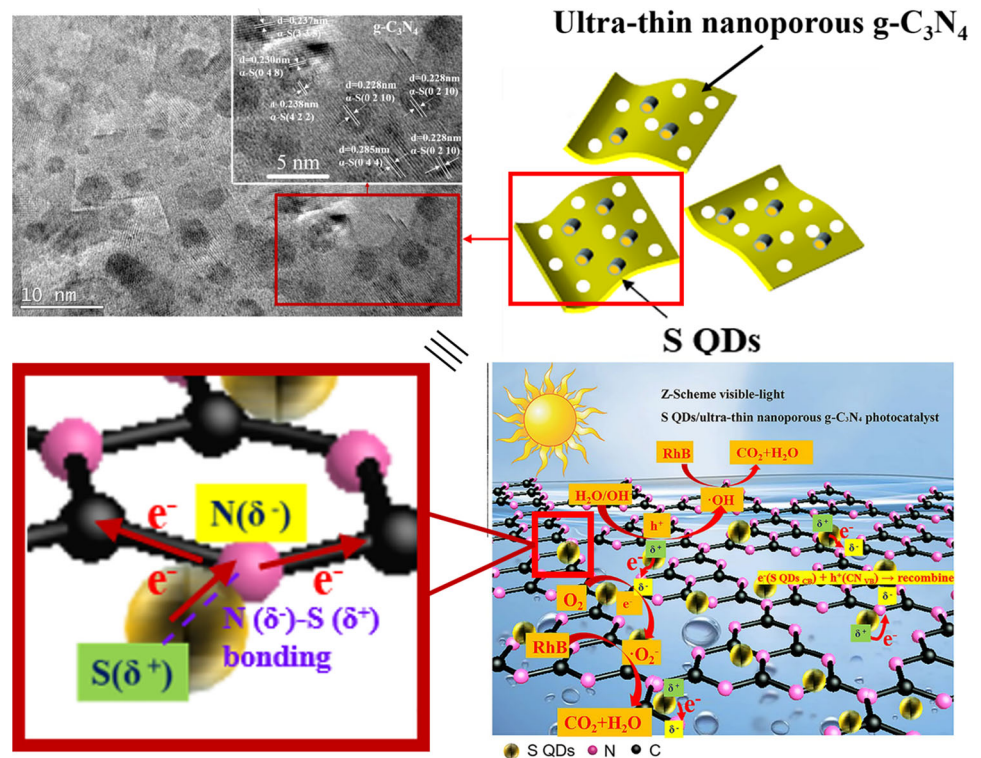
ABSTRACT

The replacing and surpassing of some functions of traditional metal-based photocatalysts by low-cost and high-efficiency non-metal semiconductor materials have become a research hotspot in functional materials. In this paper, the ultra-thin nanoporous g-C₃N₄ nanosheets were successfully embedded with highly dispersed S quantum dots (S QDs) by ultrasonic-assisted in-situ growth method, which originates from the disproportionation reaction of sodium thiosulfate. The formation of the composite was proved by XRD, XPS, AFM, TEM and HRTEM and proved that S QDs with a size of 1–3.5 nm were uniformly embedded in the surface of ultra-thin nanoporous g-C₃N₄, in which a tight and uniform 0D/2D heterojunction structure was designed and built. Meanwhile, the photocatalytic mechanism was investigated. It showed that the tight Z-Scheme heterojunction structure formed between S QDs and g-C₃N₄ improved the redox activity as well as the transfer ability of photogenerated electron holes. The system exhibited excellent photocatalytic efficiency that the complete degradation of RhB was achieved within 90 min under visible-light irradiation and revealed high stability. We believe that this research is important for the development of low-cost and efficient non-metal photocatalysts.

Handling Editor: Pedro Camargo.

Address correspondence to E-mail: liujj@mail.buct.edu.cn

GRAPHICAL ABSTRACT



Introduction

Energy conservation and environmental protection have gradually become the requirement of sustainable development in today's society. Low-cost, abundant and easily accessible non-metal photocatalysts, such as graphitic carbon nitride (g-C₃N₄), non-metal element semiconductors (S, Si, P, Se) and boron-containing materials (boron nitride), could decrease the economic and environmental costs of potential metallic secondary pollution [1]. Thanks to the suitable band structure, significant advances have been achieved to identify photocatalysts alternative to traditional metal-containing photocatalysts and show similar or higher photocatalytic performance, which is economic and workable in the current study [2]. For example, Ong et al. [3] constructed a 2D/2D reduced graphene oxide (rGO)/g-C₃N₄ nanostructure, and the photocatalytic reduction rate of CO₂ to

CH₄ was 13.93 μmol g⁻¹ h⁻¹ under a daylight bulb, which showed a better activity than Pt@CeO₂/3D CN photocatalyst [4] (the maximum photocatalytic CO₂ activity of 3.03 μmol h⁻¹ g⁻¹ for CH₄ under UV light irradiation). Luo et al. [5] prepared ultrathin sulfur-doped holey g-C₃N₄ nanosheets as visible-light-driven photocatalyst, and its hydrogen evolution rate was 6225.4 μmol h⁻¹ g⁻¹, which was 10 times higher than 1.0 wt% Pt/g-C₃N₄ [6].

Among the non-metal materials, the two-dimensional graphitic carbon nitride (g-C₃N₄) is a cheap visible-light-driven photocatalyst with high physicochemical stability and suitable band gap, which is one of the hottest research materials in recent years [7–10]. Constructing efficient non-metal g-C₃N₄-based composites instead of metal-based materials has become a general trend. The application of non-metallic elemental semiconductors with narrow band gap, such as S [13], P [11], Si [12], Se [13], B [14], has

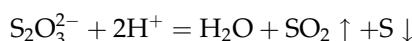
attracted widespread attention since they are abundant, cost-effective and eco-friendly [15]. The visible-light-responsive α -sulfur has attracted lots of attention due to its good photostability, suitable band gap and earth-abundant [16]. Recently, Chang et al. [17] reported the preparation of micron-sized S particles/ $g\text{-C}_3\text{N}_4$ heterostructures by using solvent evaporation method, and the degradation rate of rhodamine B within 180 min under visible light was 90%. Bankole et al. [18] modified $g\text{-C}_3\text{N}_4$ with S nanoparticles, and the photocatalytic reduction conversion yield of Cr (VI) has reached 98.8% within 15 min. However, the agglomeration of S particles and the inefficient loading results in unsatisfactory photocatalytic activity. Therefore, it is necessary to construct a tight and uniform heterojunction between S and $g\text{-C}_3\text{N}_4$, in which a smaller particle size S should be adopted.

Reducing the dimension and size of materials is beneficial for increasing the specific surface area, exposing more active sites as well as adjusting band gap structure so as to facilitate photocatalytic performance [19]. As one of the elemental quantum dot materials, S quantum dots (S QDs) have been investigated in recent years. It could be used as sensors [20], cell imaging [21], light-emitting devices [22], catalysts [23] and so on. In 2014, S QDs was prepared for the first time by phase interface reaction [23], and the SQDs/ TiO_2 composite showed a photocatalytic hydrogen evolution rate of about 191 times higher than TiO_2 under ultraviolet light, which proved that S QDs can be used as a new type of non-metal photocatalyst. However, this special mechanism for the substantially enhanced photocatalytic performance has not been explored, and the subsequent application of S QDs in photocatalysis has scarcely been reported.

In this paper, a simple ultrasonic-assisted in-situ growth method was adopted to construct a system that highly dispersed S quantum dots (1–3.5 nm) were embedded in ultra-thin nanoporous $g\text{-C}_3\text{N}_4$ tightly and uniformly. The preparation and morphology of the S QDs/ $g\text{-C}_3\text{N}_4$ composite were systematically studied, and the degradation of RhB was used to evaluate the photocatalytic performance and stability. At the same time, the photocatalytic mechanism was proposed.

Materials and methods

The ultra-thin nanoporous $g\text{-C}_3\text{N}_4$ (LN CN) is prepared by oxygen etching and liquid nitrogen treatment method based on conventional thermolysis of melamine. A simple ultrasonic-assisted in-situ growth method is used to prepare the S QDs/ $g\text{-C}_3\text{N}_4$ (S QDs/LN CN) system (Fig. 1) by the disproportionation reaction of sodium thiosulfate under acidic conditions. The preparation reaction equation is as follows:



According to the literature [24], S QDs are synthesized by the fission-self-assembly of sublimed sulfur. The detailed preparation steps are given in the Supporting Information.

Results and discussion

Characterization of S QDs/CN composite

The crystal structures of the samples are identified by XRD (Fig. 2a). Both Bulk CN and LN CN show the diffraction peaks at 13.1° and 27.4° , which are indexed to (100) and (002) of $g\text{-C}_3\text{N}_4$ indicating the in-plane ordering of the graphite-like sequence and interlayer stacking of the conjugated aromatic system in CN, respectively. Compared with Bulk CN, the (100) peak and (002) peak of LN CN are significantly reduced and broadened, which verify that LN CN has less interlayer stacking [25]. The (100) peak of LN CN shifts to higher degree after the liquid nitrogen treatment means the increased interlayer distance. It is due to the intercalation of N_2 crystals in between sheets, which also help in the exfoliation [26]. In addition, S QDs/LN CN showed characteristic peaks corresponding to $\alpha\text{-S}$ (PDF-#78-1888) and $g\text{-C}_3\text{N}_4$. This proves the truth that S QDs are loaded on LN CN nanosheets as co-catalyst instead of dopant. It is worth noting that the composite shows a significant peak shift, which can be attributed to the chemical coupling between LN CN and S QDs (Fig. 2b) [27]. The similar infrared absorption shows that the $g\text{-C}_3\text{N}_4$ maintains the typical plane conjugate structure after being exfoliated and loaded with S QDs (Fig. S1).

The surface chemical composition and states of the as-prepared composite are analyzed by X-ray

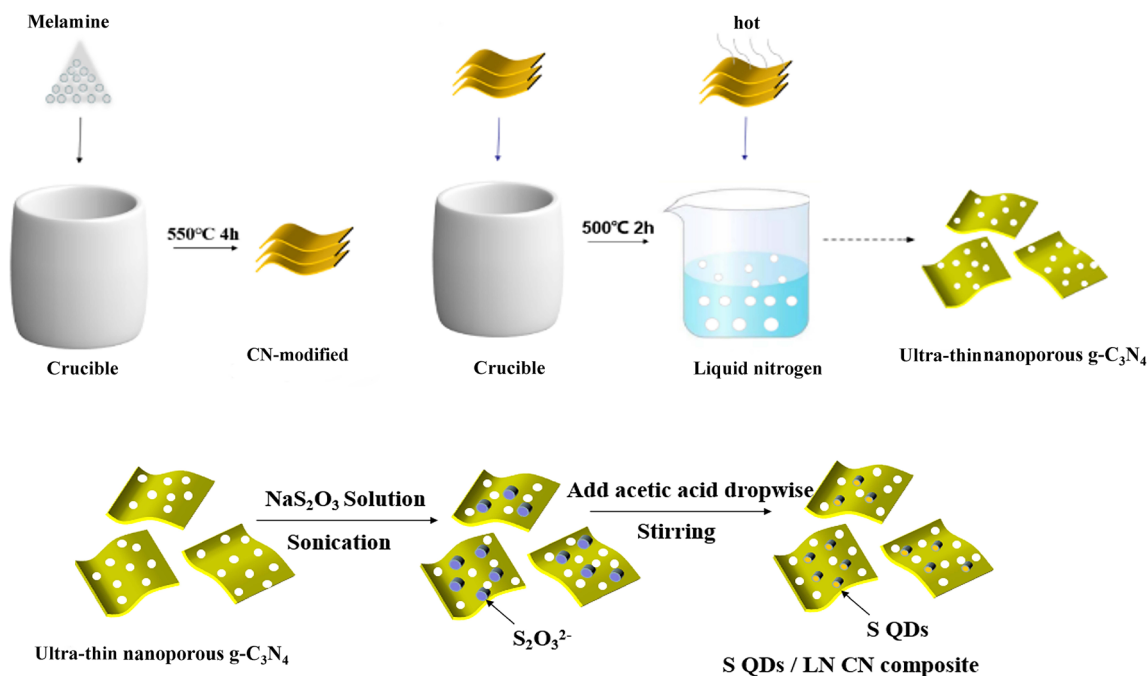


Figure 1 Schematic illustration of ultra-thin nanoporous g-C₃N₄ and S QDs/LN CN composite synthesis.

photoelectron spectroscopy (XPS) measurement (Fig. 2c–e). The C1s spectrum is deconvoluted into two distinct peaks, the peak at 288.1 eV and 284.8 eV corresponding to N–C=N groups and C–C bonding. The peaks were found at 398.8 eV and 400.5 eV in the N 1s spectrum which attributed to the sp² coordinated N(C–N=C) in the triazine ring and bridging N atom (N–(C)₃), respectively [28]. It is very clear that the S 2p spectrum shows two individual peaks at 163.5 eV and 164.6 eV, which are assigned to S–C and S–N bonds [30–32], respectively. The signal at 168.7 eV is attributed to the sulfur of SO₂[−] (2p^{1/2}) or SO₃[−] (2p^{2/3}) due to the abundant sulfite and sulfonyl/sulfonate groups on the surfaces of S QDs [23]. It is worth noting that compared with the peaks of pure CN and S, the binding energies of the C and N peaks decreased by 0.2 eV and 0.3 eV, respectively, and the peaks of S migrated to higher (0.7 eV) binding energy in S QDs/LN CN, indicating the increased and decreased charge density of CN and S, which can be explained as the migrating of electrons to N with higher electronegativity under the action of inductive effect, and the electrons also tend to delocalize to the π-conjugated triazine ring of CN; thereby, the charge density of C is increased [33, 34]. Such covalent N (δ[−])-S (δ⁺) bonding provides a favorable highway for the charge transferring, and efficient charge

separation is induced [33]. However, there is no obvious coupling effect ever been found in the composite system of Bulk CN and S particles [17, 18], indicating that both reducing the particle size of S and constructing CN with porous structure and decreased thickness are important for the coupling.

Figure 2f illustrates the N₂ adsorption–desorption isotherms and pore size analysis. All samples are identified as typical type IV isotherm with H3 hysteresis loop, which confirms the existence of mesoporous structure. The obtained BET specific surface areas of different samples are summarized in Table 1 (SI). The specific surface area of CN-modified and ultra-thin nanoporous LN CN is approximately 2.35 and 22.5 times than that of Bulk CN. This is mainly attributable to the fact that the interlayer hydrogen bond can be oxidized and broken through a more adequate contact with oxygen during the thermal treated process, and the layers are partially exfoliated [35]. After the subsequent liquid nitrogen treatment, the thickness of g-C₃N₄ is further decreased and the nanoporous structure is formed. It is clear that the BET surface area decreases from 69.45 to 13.98 m²/g as the loading ratio of S QDs increases from 10 to 50 wt%. This may originate from the re-stacking of g-C₃N₄ nanosheets, and the anchoring of S QDs occupies the originally exposed nanopore structure. As Fig. 2f presents, the BJH pore size distribution

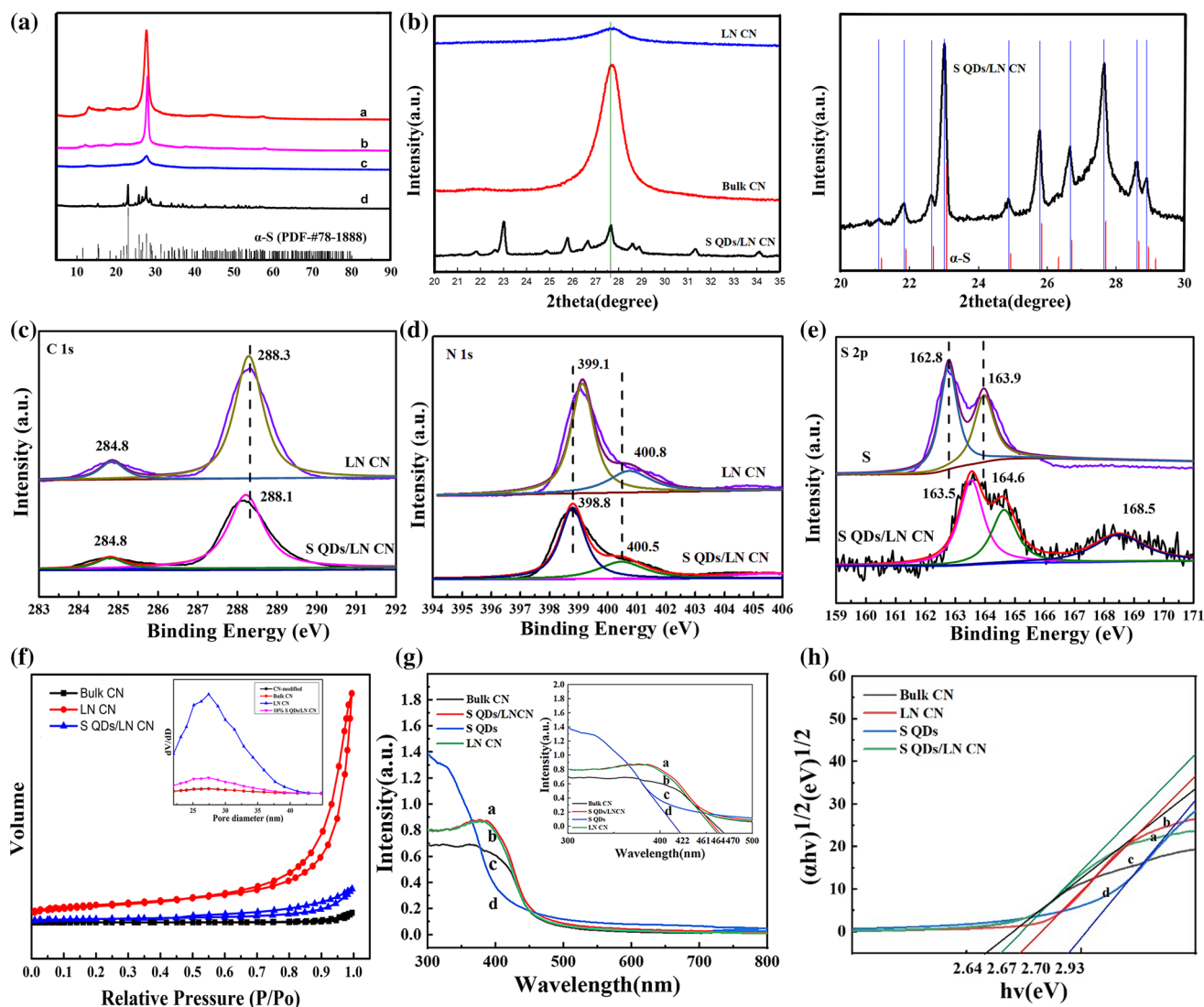


Figure 2 a, b XRD spectra of a. Bulk CN b. CN-modified c. LN CN d. S QDs/LN CN; c–e XPS survey spectra and high-resolution XPS spectra of the S QDs/LN CN composite; f N₂ adsorption–desorption isotherms and the corresponding pore size distribution

curve of LN CN shows a large intensity of peak in the range of 25–30 nm, and the sharp peak appears at 27 nm. It indicates that the ultra-thin nanoporous CN nanosheets with large specific surface area have been successfully prepared by oxygen etching and liquid nitrogen treatment. After being loaded with S QDs, the curves tend to be flat, which can be ascribed the fact that S QDs partially occupy the pores of LN CN according to decrease in BET surface area (195.74–69.45 m²/g).

Ultraviolet visible diffuse reflectance spectroscopy (UV–Vis DRS) analysis is performed to evaluate the optical properties of the photocatalysts, and the

curves of the samples (inset); g UV–vis diffuse spectra and h corresponding Tauc plot spectra of a. S QDs/LN CN composite b. LN CN, c. Bulk CN and d. S QDs.

corresponding optical band gaps are estimated from the Tauc-plot (Fig. 2g, h). The band gap energies (E_g) of as-prepared samples have been calculated applying Tauc's equation, Eq. 1 [36]:

$$(\alpha h\nu)^{1/2} = A (h\nu - E_g) \quad (1)$$

where A, h, E_g , α and ν are the absorption constant, Planck's constant, band gap energy, absorption coefficient and frequency, respectively. As shown in Fig. 2h, the E_g values of as-prepared LN CN and S QDs are 2.70 and 2.93 eV. It is clearly found that the light absorption intensity of LN CN within 470 nm is promoted on account of the multiple reflection of

incident light in nanoporous structures which increases the effective path length for light absorption [37]. Meanwhile, the absorption edge displays a slightly blue-shifted due to the quantum confinement effect [38]. Both S QDs/LN CN and LN CN appear similar light absorption tendency, which was due to the low content of S. The absorption edge undergoes a slight red shift, and the absorption intensity is mildly increased after compounding.

The microstructure is observed by transmission electron microscope (TEM), and the results are shown in Fig. 3. Compared with Bulk CN, the ultra-thin nanoporous two-dimensional flake-like structures are obtained after oxygen etching and liquid nitrogen treatment (Fig. 3a, b), indicating that the Bulk CN was successfully exfoliated as we desired. This is further evaluated via atomic force microscopy (AFM) analysis (Fig. 3c), which show the LN CN flakes are composed of nanosheets with a thickness range from 0.5 to 1.8 nm corresponding to the layer number of

1–3 [38]. In Fig. 3d, it is observed that re-stacking and curling occurred during the compounding process, and many S quantum dots (1–3.5 nm) were embedded in the surface of the g-C₃N₄ nanosheets uniformly and effectively (Fig. S2). Meanwhile, the crystallinity phase of the material can be scrutinized by observing the high-resolution TEM (HRTEM) image. Well-crystallized S QDs were clearly observed to be embedded in g-C₃N₄ with different crystal planes, such as the lattice fringes spacing of 0.228, 0.230, 0.237, 0.238 and 0.285 nm assigned as the (0 2 10), (0 4 8), (3 3 5), (4 2 2) and (0 4 4) crystal planes of α -S (PDF-#78-1888), respectively. Besides, the corresponding energy-dispersive spectrometer (EDS) mapping (Fig. 3g–k) confirms the uniform distribution of C, N, O and S. Due to the easy evaporation of S under electron beam with high energy at high magnification [39] and limitations of the selection area, the elemental mapping of S is not obvious. Scanning electron microscope (SEM)-EDS analysis

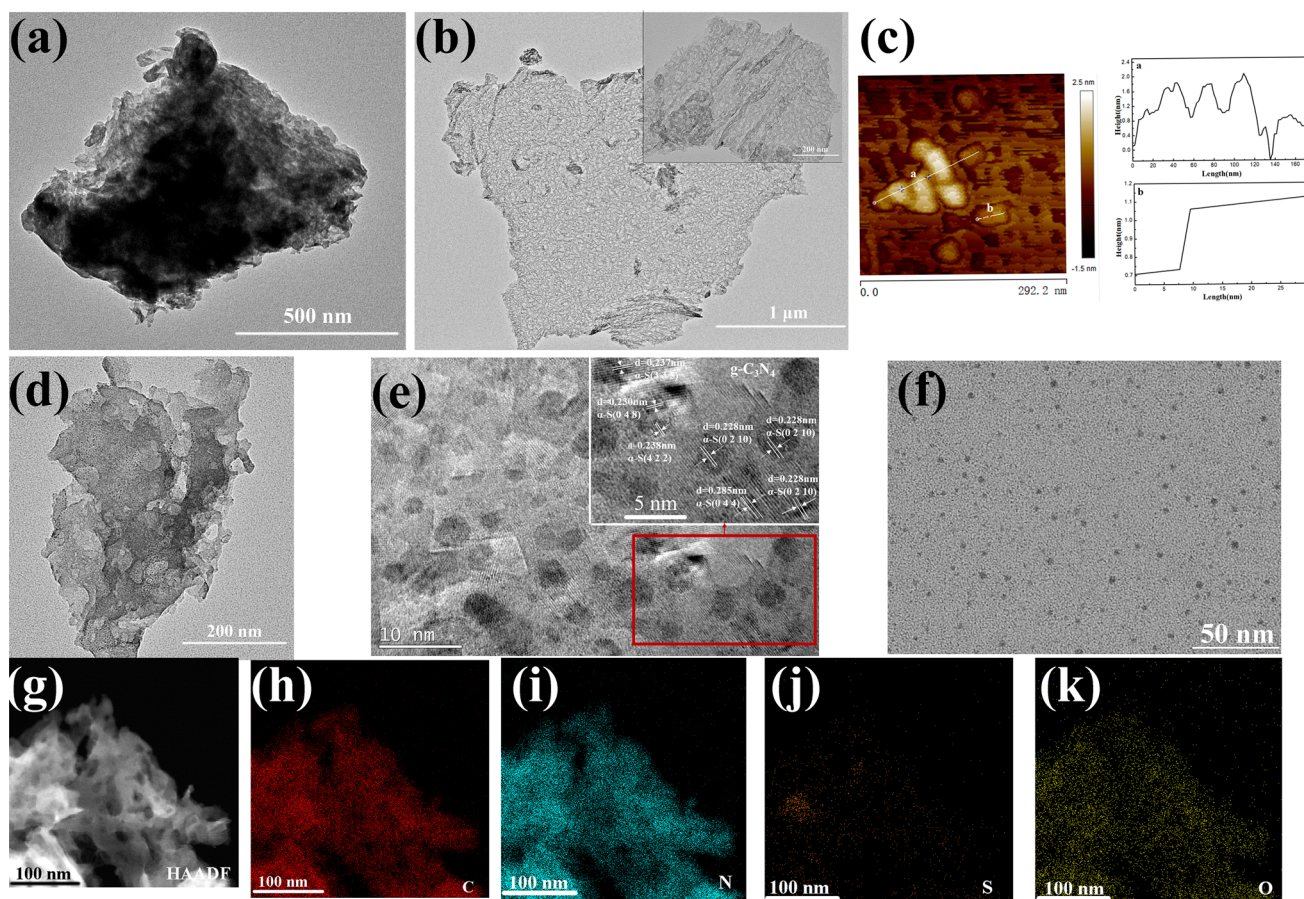


Figure 3 TEM images of **a** Bulk CN, **b** LN CN, **c** AFM image of the LN CN, **d** 10% S QDs/LN CN, **f** S QDs, **e** HRTEM images of the S QDs/LN CN composite, **g–k** energy-dispersive spectroscopy and the corresponding mapping of the S QDs/LN CN composite.

with lower electron beam energy is adopted to further proves the successful loading of S, which shows the content of S is 9.67 wt% (Fig. S3). Such structure is speculated to be related to the large specific surface area and nanoporous structure of LN CN, as well as the bonding between S and CN which contribute to the high-dispersion anchoring of the S QDs on the substrate.

Evaluation of photocatalytic activity of S QDs/CN composite

The degradation of RhB under visible light is carried out to evaluate the photocatalytic performance (Fig. 4a, b, Fig. S5a). The photocatalytic activity order of the samples is 10% S QDs/LN CN > LN CN > CN-modified > LN-Bulk CN > Bulk CN. LN CN exhibits stronger adsorption activity and enhanced visible-light photocatalytic activity than Bulk CN. The BET surface area of LN CN is about 22.5 times of Bulk CN, which results in the increase in active sites of $g\text{-C}_3\text{N}_4$, and the quantum confinement effect also leads to the enhanced oxidation and reduction performance of photogenerated holes and electrons [38].

In the composite system, the photocatalytic rate is maximized at the S QDs content of 10 wt% and 100% degradation of RhB can be completed within 90 min after adsorption equilibrium, and with the increase in the loading rate, the photocatalytic activity decreases. This is because the excessive loading of S QDs inflicts the agglomeration of quantum dots (Fig. S4), which adversely affects the photocatalytic efficiency. The activity of LN CN is 4.1 times of Bulk CN, and the catalytic rate of 10% S QDs/LN CN is about 2.5 times higher than that of LN CN, which can be profit from the ultra-thin nanoporous structure of LN CN as well as the tight coupling between LN CN and S QDs. To avoid the possibility of photosensitization effect, the phenol (100 ml, 10 mg/L) is adopted as a colorless reagent, and the degradation curve is shown in Fig. S5b. The photoluminescence intensity of different samples is measured at the excitation wavelength of 370 nm to characterize the trapping and transfer efficiency of photo-excited electron-hole pairs. As shown in Fig. 4c, the PL peak intensities of Bulk CN, CN-modified, LN CN and S QDs/LN CN decrease successively, and the emission peaks appear blue-shifted because of the efficient separation and

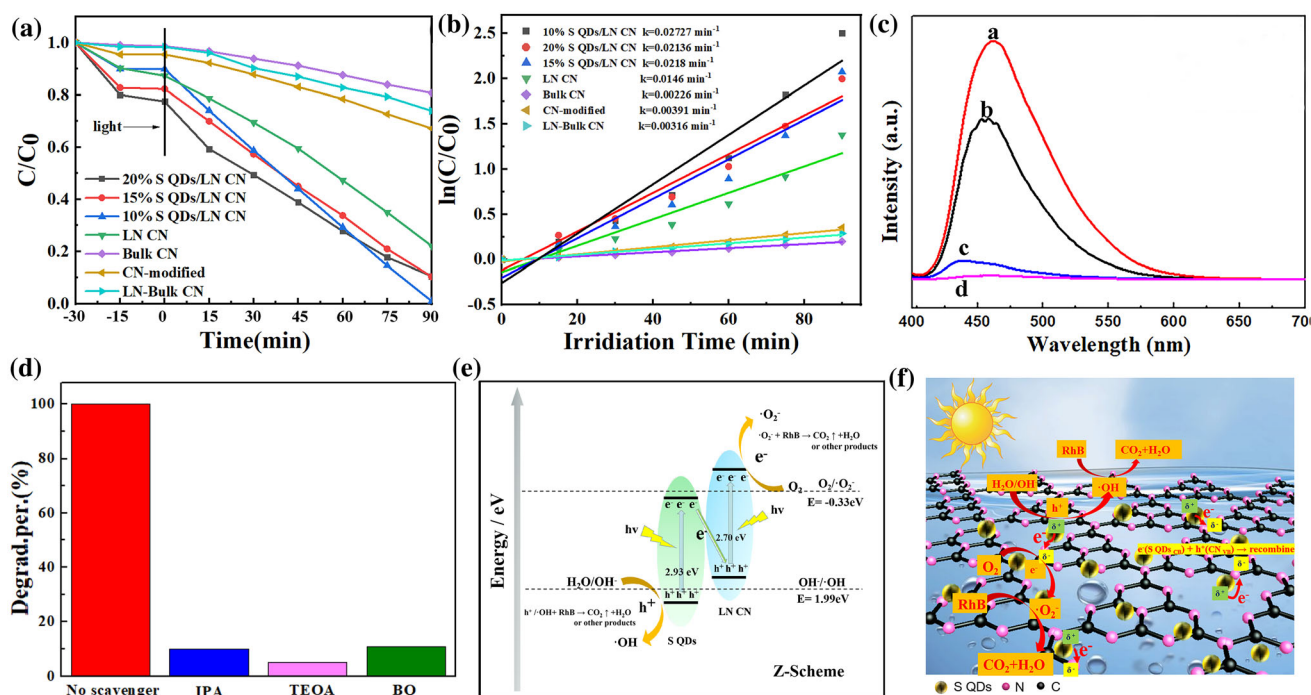


Figure 4 a Photocatalytic degradation of RhB and b the corresponding reaction rate curves for different samples under visible light c PL spectra of a. Bulk CN, b. CN-modified, c. LN CN and d. S QDs/LN CN composite d effect of different

scavengers on the RhB degradation in the presence of S QDs/LN CN and e, f schematic of photogenerated charge transfer in the S QDs/LN CN under visible light.

migration of photogenerated charge carriers and the quantum confinement effect induced by the reduction in thickness [38]. A rapidly quenched PL intensity is showed in S QDs/LN CN, indicating that the efficient separation of photogenerated carriers was successfully achieved. The excellent stability of S QDs/LN CN is investigated by cycling test (Fig. S6). The better performance of the composite is mainly discussed in the following aspects. Firstly, the ultra-thin nanoporous g-C₃N₄ nanosheets with higher specific surface area (195.74 m²/g) provide more active sites and facilitate the in-situ growth and anchoring of S QDs on the surface. Secondly, the ultra-thin structure can shorten the distance of photogenerated carriers migrated from the interior to the surface, thereby increasing the carriers' migration rate and reducing the recombination rate [38]. Thirdly, the N (δ⁻)-S (δ⁺) bonds formed between S QDs and g-C₃N₄ play a crucial role in transferring photogenerated electrons; thus, the migration of photogenerated charge carriers is effectively promoted.

Mechanism of photocatalytic activity

Based on the above analysis, the photocatalytic mechanism estimation is illustrated. In pure systems, the potentials of conduction band (CB) and valence band (VB) edges can be calculated by Mulliken electronegativity theory, using Eqs. 2 and 3:

$$E_{CB} = X - E_e - 0.5E_g \quad (2)$$

$$E_{VB} = E_{CB} + E_g \quad (3)$$

where E_{CB} , E_{VB} and X are the conduction band, valence band energies and the geometric average of the electro-negativities of the component atoms, respectively. E_g and E_e are the band gap and the free-electron energy of ≈ 4.5 eV on the hydrogen scale, respectively [36]. The valence band and conduction band edge values of LN CN are calculated to be 1.57 eV and -1.13 eV, respectively. Compared with g-C₃N₄, S QDs show lower conduction band energy and higher valence band energy [23, 35, 40]. Triethanolamine (TEOA), isopropanol (IPA) and benzoquinone (BQ) are adopted as the scavengers for photogenerated holes (h^+), hydroxyl radical ($\cdot OH$) and superoxide radical ($\cdot O_2^-$), respectively. The results showed that the three scavengers have an obvious inhibitory effect on the photocatalytic degradation of RhB (Fig. 4d), indicating that $\cdot OH$, h^+

and $\cdot O_2^-$ are the main active substances. Compared with g-C₃N₄ (+ 1.57 eV), the valence potential of S QDs is positive enough to oxidize OH^- to $\cdot OH$ ($E(\cdot OH/OH^-) = +1.99$ eV) [41]. However, the E_{CB} of S QDs could not reach -0.33 eV ($E(\cdot O_2^-/O_2) = -0.33$ eV), which is not negative enough to reduce O_2 to $\cdot O_2^-$. So, the forming of $\cdot O_2^-$ is mainly realized on the conduction band (-1.13 eV) of LN CN with higher reduction ability. In conclusion, it can be judged that $\cdot OH$ is mainly formed in the valence band of S QDs and the forming of $\cdot O_2^-$ ($E(\cdot O_2^-/O_2) = -0.33$ eV) is mainly realized on the conduction band (-1.13 eV) of LN CN with higher reduction ability synchronously. Therefore, it is inferred that a direct Z-Scheme heterojunction structure is formed between S QDs and LN CN (Fig. 4e). The mechanism is analyzed as follows: Under the excitation of visible light, the photogenerated electrons of S QDs and LN CN in valence band transfer to conduction band, and accordingly, photogenerated holes formed. After constructing direct Z-scheme system, the S QDs/LN CN featured the system to involve the capture of photogenerated electrons in the CB of S QDs by the VB of LN CN through the N (δ⁻)-S (δ⁺) coupling. Benefitted from the Z-scheme process, more electrons and holes with higher redox performance were survived and leading to an excellent activity [42]. The tight bonding contributes to the stably embedding of S QDs on the substrate and serves as a highway [33] to promote the transfer and separation of electrons, which facilitates the formation of Z-Scheme simultaneously. Compared with the traditional ternary indirect Z-Scheme system including two semiconductors with different energy gaps and noble metals as electron mediators, this system adopts the bonding between non-metal semiconductors to promote the transportation of electrons and constructs the direct Z-Scheme system [42]. The composite exhibits excellent photocatalytic activity under visible light.

Conclusions

In this paper, S QDs are uniformly embedded in ultra-thin nanoporous g-C₃N₄ via a simple ultrasonic-assisted in-situ growth method. Due to chemical bonding, S QDs with a size of 1–3.5 nm are uniformly embedded in the ultra-thin nanoporous g-C₃N₄. Meanwhile, it is well documented that a compact direct Z-scheme nano-heterojunction structure is

formed. As a result, the S QDs/LN CN samples exhibited superior photocatalytic activity for RhB degradation under visible light compared to bulk g-C₃N₄ because of the tight coupling of S QDs and LN CN and the forming of direct Z-scheme heterojunction, and it still maintains superior stability after four cycles. The easily bonding effect among the non-metal materials may be an apt option for studying the construction of heterojunctions based on non-metallic elements, promoting the effective separation and transport of photogenerated carriers and enhancing the catalytic performance.

Acknowledgements

This work was financially supported by the Natural Science Foundation of China under Grant No. 10972025.

Author contributions

Yimeng Wang contributed to conceptualization, methodology, investigation, writing draft. Jianjun Liu contributed to resources, supervision, writing, review and editing. Hecheng Ma, Xiangdong Zhang and Shuxiang Zheng contributed to investigation and data curation. Yingchun Yu contributed to the characterization. Shengli Zuo contributed to supervision. All authors read and contributed to the manuscript and discussed the results.

Data availability

All relevant data presented in the article are stored according to institutional requirements and as such are not available online. However, all data used in this manuscript can be made available upon request to the authors.

Declarations

Conflict of interest There are no conflict to declare.

Supplementary Information: The online version contains supplementary material available at <http://doi.org/10.1007/s10853-021-06624-4>.

References

- [1] Wang W, Yu JC, Xia D, Wong PK, Li Y (2013) Graphene and g-C₃N₄ nanosheets cowrapped elemental α -sulfur as a novel metal-free heterojunction photocatalyst for bacterial inactivation under visible-light. *Environ Sci Technol* 47(15):8724–8732
- [2] Shen H, Peppel T, Strunk J, Sun Z (2020) Photocatalytic reduction of CO₂ by metal-free-based materials: recent advances and future perspective. *Sol RRL* 4(8):1900546
- [3] Ong W-J, Tan L-L, Chai S-P, Yong S-T, Mohamed AR (2015) Surface charge modification via protonation of graphitic carbon nitride (g-C₃N₄) for electrostatic self-assembly construction of 2D/2D reduced graphene oxide (rGO)/g-C₃N₄ nanostructures toward enhanced photocatalytic reduction of carbon dioxide to methane. *Nano Energy* 13:757–770
- [4] Zhao X, Guan J, Li J, Li X, Wang H, Huo P, Yan Y (2021) CeO₂/3D g-C₃N₄ heterojunction deposited with Pt cocatalyst for enhanced photocatalytic CO₂ reduction. *Appl Surf Sci* 537:147891
- [5] Luo L, Gong Z, Ma J, Wang K, Zhu H, Li K, Xiong L, Guo X, Tang J (2021) Ultrathin sulfur-doped holey carbon nitride nanosheets with superior photocatalytic hydrogen production from water. *Appl Catal B* 284:119742
- [6] Han C, Su P, Tan B, Ma X, Lv H, Huang C, Wang P, Tong Z, Li G, Huang Y (2021) Defective ultra-thin two-dimensional g-C₃N₄ photocatalyst for enhanced photocatalytic H₂ evolution activity. *J Colloid Interf Sci* 581:159–166
- [7] Li K, Zhang M, Ou X, Li R, Li Q, Fan J, Lv K (2021) Strategies for the fabrication of 2D carbon nitride nanosheets. *Wuli Huaxue Xuebao*. <https://doi.org/10.3866/PKU.WHXB202008010>
- [8] Kadam AN, Moniruzzaman M, Lee S-W (2019) Dual functional S-doped g-C₃N₄ pinhole porous nanosheets for selective fluorescence sensing of Ag⁺ and visible-light photocatalysis of dyes. *Molecules* 24(3):450
- [9] Kadam AN, Kim H, Lee S-W (2020) Low-temperature in situ fabrication of porous S-doped g-C₃N₄ nanosheets using gaseous-bubble template for enhanced visible-light photocatalysis. *Ceram Int* 46(18):28481–28489
- [10] Babu B, Shim J, Kadam A, Yoo K (2019) Modification of porous g-C₃N₄ nanosheets for enhanced photocatalytic activity: in-situ synthesis and optimization of NH₄Cl quantity. *Catal Commun* 124:123–127
- [11] Cao Q, Guo M, Cao J, Lin H, Chen Y, Chen S (2019) An elemental S/P photocatalyst for hydrogen evolution from water under visible to near-infrared light irradiation. *Chem Commun* 55(87):13160–13163
- [12] Kang Z, Tsang CHA, Wong N-B, Zhang Z, Lee S-T (2007) Silicon quantum dots: a general photocatalyst for reduction,

- decomposition, and selective oxidation reactions. *J Am Chem Soc* 129(40):12090–12091
- [13] Chiou Y-D, Hsu Y-J (2011) Room-temperature synthesis of single-crystalline Se nanorods with remarkable photocatalytic properties. *Appl Catal B* 105(1–2):211–219
- [14] Liu G, Yin LC, Niu P, Jiao W, Cheng HM (2013) Visible-light-responsive β -rhombohedral boron photocatalysts. *Angew Chem Int Ed* 52(24):6242–6245
- [15] Liu G, Niu P, Cheng HM (2013) Visible-light-active elemental photocatalysts. *ChemPhysChem* 14(5):885–892
- [16] Hu C, Zheng S, Lian C, Chen F, Lu T, Hu Q, Duo S, Zhang R, Guan C (2015) α -S nanoparticles grown on MoS₂ nanosheets: a novel sulfur-based photocatalyst with enhanced photocatalytic performance. *J Mol Catal A Chem* 396:128–135
- [17] Chang F, Yan W, Cheng W, Wu F, Deng B, Hu X (2018) The construction and enhanced photocatalytic performance of binary composite S/g-C₃N₄. *Mater Sci Semicond Process* 87:1–6
- [18] Bankole OM, Olorunsola TD, Ogunlaja AS (2021) Photocatalytic decontamination of toxic hexavalent chromium in water over graphitic carbon nitride supported sulfur nanoparticles. *J Photochem Photobiol A* 405:112934
- [19] Wang T, Liu X, Men Q, Ma C, Liu Y, Liu Z, Huo P, Li C, Yan Y (2018) Green synthesis g-C₃N₄ quantum dots loading h-BN for efficient and stable photocatalytic performance. *J Mol Liq* 268:561–568
- [20] Tan Q, An X, Pan S, Liu H, Hu X (2021) Hydrogen peroxide assisted synthesis of sulfur quantum dots for the detection of chromium (VI) and ascorbic acid. *Spectrochim Acta Part A* 247:119122
- [21] Song Y, Tan J, Wang G, Gao P, Lei J, Zhou L (2020) Oxygen accelerated scalable synthesis of highly fluorescent sulfur quantum dots. *Chem Sci* 11(3):772–777
- [22] Xu N, Wen Q (2021) Single element material sulfur quantum dots nonlinear optics and ultrafast photonic applications. *Opt Laser Technol* 138:106858
- [23] Li S, Chen D, Zheng F, Zhou H, Jiang S, Wu Y (2014) Water-soluble and lowly toxic sulphur quantum dots. *Adv Funct Mater* 24(45):7133–7138
- [24] Shen L, Wang H, Liu S, Bai Z, Zhang S, Zhang X, Zhang C (2018) Assembling of sulfur quantum dots in fission of sublimed sulfur. *J Am Chem Soc* 140(25):7878–7884
- [25] Lin Q, Li L, Liang S, Liu M, Bi J, Wu L (2015) Efficient synthesis of monolayer carbon nitride 2D nanosheet with tunable concentration and enhanced visible-light photocatalytic activities. *Appl Catal B* 163:135–142
- [26] Wang H, Lv W, Shi J, Wang H, Wang D, Jin L, Chao J, van Aken PA, Chen R, Huang W (2019) Efficient liquid nitrogen exfoliation of MoS₂ ultrathin nanosheets in the pure 2H phase. *ACS Sustain Chem Eng* 8(1):84–90
- [27] Wu D, Chen W, Wang X, Fu X-Z, Luo J-L (2020) Metal-support interaction enhanced electrochemical reduction of CO₂ to formate between graphene and Bi nanoparticles. *J CO₂ Util* 37:353–359
- [28] Dong F, Li Y, Wang Z, Ho W-K (2015) Enhanced visible light photocatalytic activity and oxidation ability of porous graphene-like g-C₃N₄ nanosheets via thermal exfoliation. *Appl Surf Sci* 358:393–403
- [29] Xu Z, Yao K, Li Z, Fu L, Fu H, Li J, Cao L, Huang J (2018) Sulfur nanodots as MoS₂ antiblocking agent for stable sodium ion battery anodes. *J Mater Chem A* 6(22):10535–10542
- [30] Fan Q, Liu J, Yu Y, Zuo S, Li B (2017) A simple fabrication for sulfur doped graphitic carbon nitride porous rods with excellent photocatalytic activity degrading RhB dye. *Appl Surf Sci* 391:360–368
- [31] Hong J, Xia X, Wang Y, Xu R (2012) Mesoporous carbon nitride with in situ sulfur doping for enhanced photocatalytic hydrogen evolution from water under visible light. *J Mater Chem* 22(30):15006–15012
- [32] Ye L, Wang D, Chen S (2016) Fabrication and enhanced photoelectrochemical performance of MoS₂/S-doped g-C₃N₄ heterojunction film. *ACS Appl Mater Interf* 8(8):5280–5289
- [33] Cheng C, Zong S, Shi J, Xue F, Zhang Y, Guan X, Zheng B, Deng J, Guo L (2020) Facile preparation of nanosized MoP as cocatalyst coupled with g-C₃N₄ by surface bonding state for enhanced photocatalytic hydrogen production. *Appl Catal B* 265:118620
- [34] Wang J, Mao J, Zheng X, Zhou Y, Xu Q (2021) Sulfur boosting CO₂ reduction activity of bismuth subcarbonate nanosheets via promoting proton-coupled electron transfer. *Appl Catal B*. <https://doi.org/10.1016/j.apsusc.2021.150197>
- [35] Niu P, Zhang L, Liu G, Cheng HM (2012) Graphene-like carbon nitride nanosheets for improved photocatalytic activities. *Adv Funct Mater* 22(22):4763–4770
- [36] Khan UA, Liu J, Pan J, Ma H, Zuo S, Yu Y, Ahmad A, Iqbal M, Ullah S, Li B (2019) One-pot fabrication of hierarchical floating Bi–Bi₂S₃–Bi₂WO₆/expanded perlite photocatalysts for efficient photocatalysis of organic contaminants utilized sunlike illumination. *Ind Eng Chem Res* 58(22):9286–9299
- [37] Li Y, Jin R, Xing Y, Li J, Song S, Liu X, Li M, Jin R (2016) Macroscopic foam-like holey ultrathin g-C₃N₄ nanosheets for drastic improvement of visible-light photocatalytic activity. *Adv Energy Mater* 6(24):1601273
- [38] Yang Y, Zhang D, Fan J, Liao Y, Xiang Q (2021) Construction of an Ultrathin S-scheme heterojunction based on few-layer g-C₃N₄ and monolayer Ti₃C₂T_x MXene for photocatalytic CO₂ reduction. *Sol RRL* 5(2):2000351

- [39] Wang Z, Zhang C, Wang H, Xiong Y, Yang X, Ye S, Rogach AL (2020) Two-step oxidation synthesis of sulfur with a red aggregation-induced emission. *Angew Chem* 132(25):10083–10088
- [40] Zhang M, Lin H, Cao J, Guo X, Chen S (2017) Construction of novel S/CdS type II heterojunction for photocatalytic H₂ production under visible light: the intrinsic positive role of elementary α -S. *Chem Eng J* 321:484–494
- [41] Liu G, Niu P, Yin L, Cheng H-M (2012) α -Sulfur crystals as a visible-light-active photocatalyst. *J Am Chem Soc* 134(22):9070–9073
- [42] Ren Y, Zeng D, Ong W-J (2019) Interfacial engineering of graphitic carbon nitride (g-C₃N₄)-based metal sulfide heterojunction photocatalysts for energy conversion: a review. *Chin J Catal* 40(3):289–319

Publisher's Note Springer Nature remains neutral with regard to jurisdictional claims in published maps and institutional affiliations.